Investigation of the unsteady Edney type IV and VII shock-shock interaction

Christian Windisch[1]†, Birgit Reinartz[2] and Siegfried Müller[3]

[1]German Research School for Simulation Sciences, RWTH Aachen University, 52056 Aachen, Germany

[2]Chair for Computational Analysis of Technical Systems, RWTH Aachen University, 52056 Aachen, Germany

[3]Institut für Geometrie und Praktische Mathematik, RWTH Aachen University, 52056 Aachen, Germany

Edney type IV and type VII shock-shock interactions are complex hypersonic flow phenomena. They are characterized by a supersonic jet which reaches far into the flow field. An experimental investigation of the inner jet structure is difficult, especially in cases where the jet is subject to high-frequency unsteady movements. The present paper provides insight into the jet structure by means of a highly-resolved Computational Fluid Dynamics analysis in thermochemical nonequilibrium. Simulations of an Edney type IV interaction in nitrogen flow are presented. Multiple resolution levels support the identification and analysis of the mechanisms of the jet unsteadiness. The second configuration is an Edney type VII interaction. This shock-shock interaction type was observed and defined in nitrogen flow by Yamamoto et al. The present results demonstrate that this interaction may also be observed in CO_2-dominated flow with a gas composition similar to the Martian atmosphere. The results provide insight into the jet structure of this less known interaction.

Key words: Hypersonic flows, shock-shock interaction, grid adaptation, thermochemical nonequilibrium.

---

1. Introduction

The proper prediction of thermal and structural loads is crucial for the design of future space transportation systems. Especially the thermal and structural loads caused by shock-shock interactions may pose significant restrictions on the overall system. Shock-shock interactions are frequently found in supersonic and hypersonic flow fields and are characterized by a wide range of relevant flow phenomena on different length scales. Pertinent examples of shock-shock interactions are the Edney type IV interaction, cf. Lind & Lewis (1995), as well as the less known Edney type VII interaction, which was defined by Yamamoto *et al.* (1999). These configurations are the result of an incident shock wave which impinges on the bow shock in front of a blunt body. A supersonic jet forms between two triple points and reaches far into the subsonic region behind the bow shock.

The Edney type IV interaction is frequently used in theoretical and experimental investigations as it leads to high aerothermal loads on the body surface. Depending on

† Email address for correspondence: windisch@igpm.rwth-aachen.de

the particular configuration, Edney type IV interactions may show unsteady phenomena. Due to their high-frequencies, these unsteady mechanisms cannot be fully captured in experiments. Therefore, highly-resolved CFD simulations are an essential means to investigate such configurations.

The Edney type VII interaction was observed for a nitrogen flow configuration and defined by Yamamoto *et al.* (1999). The supersonic jet of this type of shock-shock interaction is strongly curved. Because of the large distance between the jet and the body surface, this shock interaction leads only to moderate thermal and structural loads. However, the shock structure itself is more complex than the Edney type IV interaction as more shock interference patterns are observed.

The proper CFD simulation and prediction of the Edney type IV and type VII shock interaction patterns is a challenging task. The structure of the incident oblique shock wave and the main shock must be properly captured in order to predict the resulting shock pattern. These strong shocks are formed at a certain distance ahead of the vehicle surface and spread out over a larger area. In addition, the boundary layer and especially the wall temperature gradient need to be properly resolved in order to capture the wall heat flux and to predict the thermal loads on the vehicle surface. Strong interaction patterns, which are potentially unstable (Grasso *et al.* (2003)), can be found between the bow shock and the boundary layer. To account for the high-temperature flow field behind the shock pattern, the physical modeling of the numerical simulation must account for chemical and thermal nonequilibrium effects.

The proper spatial and temporal resolution is the key to precisely capture the shock-shock interaction pattern. Furthermore, the inherent instability of the Edney type IV and type VII shock-shock interactions is difficult for CFD solvers, especially when considering the potentially unstable solution behavior of numerical simulations in thermochemical nonequilibrium. In the present work we will employ the QUADFLOW solver (Bramkamp *et al.* (2004)), an integrated concept of grid generation, grid adaptation and nonequilibrium flow solver. The multiscale-based grid adaptation of the QUADFLOW solver produces a grid with a locally high resolution. The computational costs are kept low, as only relevant areas are refined and the whole grid is adjusted to the exact location of the flow features in the unsteady solution.

This allows to produce new highly-resolved simulation results in the present work that give new insights into the jet unsteadiness of the Edney type IV and type VII shock-shock interactions. In addition, this paper comments on the grid sensitivity of shock-shock interactions and points out potential pitfalls of misleading steady-state solutions caused by high dissipation.

The Edney type IV interaction investigated in the present work is based on an experiment in nitrogen flow by Sanderson (1995). From the experimental readings, Sanderson reported an unsteady behavior of the supersonic jet structure. As high-frequency unsteady mechanisms are difficult to measure, the following computational results are important to gain further insights. In the present simulations, the exact location of the impinging shock wave is selected within the uncertainty range of the experiment in such a way that a pronounced unsteady mechanism is observed. The grid adaptation strategy of the QUADFLOW solver allows to investigate multiple resolution levels, which support the identification and analysis of the mechanisms of the jet unsteadiness. This leads to a new classification of the unsteady flow field behaviour. An additional benefit of the multiresolution approach is the evaluation of the solution quality with respect to grid resolution. The analysis of the influence of the numerical discretization on the jet features helps to address grid sensitivities in simulations of shock-shock configurations which is an important, but underrepresented topic in the literature. In addition to the investiga-

tion of the flow field, the transient wall heat flux rates and their interdependence on the movement of the jet structure are analysed.

In the second configuration, a CO_2-dominated gas composition equal to the Martian atmosphere is investigated. Planned interplanetary space missions have risen the interest of the research community for the Martian atmosphere. This configuration provides new insight into the less known Edney type VII shock-shock interaction. In the following it will be demonstrated that this kind of shock-shock interaction, so far only reported for nitrogen, can also be observed in CO_2 gas compositions.

The present paper is organised as follows: The literature review in Section 2 familiarises the reader with shock-shock interactions. The setup of the Computational Fluid Dynamics (CFD) analysis is described in Section 3. The results of the Edney type IV and Edney type VII interactions are discussed in Sections 4 and 5, respectively.

2. Literature review

The first part of the literature review provides the reader with background information on the shock-shock interaction types considered in the present work. The second part discusses two pertinent analyses of the jet unsteady mechanism which are found in the literature. The discussion demonstrates that the exact mechanism remains unclear and is subject to the particular configuration under investigation.

2.1. *Classification of shock-shock interactions*

Shock-shock interactions have been widely discussed in the literature over the past decades. Referring to Sanderson (1995), the shock interference pattern depends on the strength and angle of the intersecting shocks, the geometry of the body around which the interference pattern is formed, the relative location of the impinging shock on the body and the gas properties, i.e., the ratio of specific heats.

The most comprehensive classification of shock-shock interactions was carried out by Edney (1968), who experimentally and theoretically investigated the impingement of an oblique shock wave on a strong bow shock in front of a blunt body. Edney distinguished six shock-interaction patterns named as types I-VI. The particular type depends on the location of the impingement on the bow shock.

The Edney type IV interaction is the most critical shock-shock interaction in terms of the aerothermal loads on the wall (Grasso *et al.* (2003)). A detailed analysis of the front section of the shock interaction pattern was carried out for double-wedge geometries by Olejniczak *et al.* (1997). A supersonic jet forms between two triple points and reaches into the subsonic region behind the bow shock. The flow bends upwards by a combination of several expansion and compression waves. The wall impingement of the flow passing though the shock pattern of the jet and the terminating shock leads to high pressures and temperatures on the surface of the blunt body. This configuration exhibits an unstable behaviour and is highly sensitive to the exact location of the shock impingement. When the impinging shock wave is moved upward, the jet begins to bend upwards along the cylinder surface. This state is frequently characterized as a type IVa interaction (Grasso *et al.* (2003)).

For a high location of the impinging shock, Yamamoto *et al.* (1999) experienced a new type of shock-shock interference which involves a *"supersonic jet streaming toward the upper downstream without stagnating on the body"*. This is in contrast to the type IVa interaction in which case the supersonic jet still touches the wall surface. Yamamoto et al. referred to this new interaction as type VII. The supersonic jet of this interaction is characterized by a strong vorticity.

2.2. *Unsteady mechanism*

The Edney type IV interaction is known as being inherently unstable. As explained in the following, different types of behaviour are found in the literature which range from fully unsteady to steady flow characteristics of the jet structure. No comprehensive systematic studies of the unsteady behaviour are known to the authors. However, the unsteady characteristics of particular configurations are subject to various publications:

Referring to Lind & Lewis (1996), the unsteadiness of the Edney type IV interaction depends strongly on the angle and strength of the oblique shock wave and its impingement location on the bow shock. They observed that small changes in the impinging shock properties may cause steady flow fields to become unsteady. Following the observation of Lind & Lewis (1996), *"the high-frequency jet unsteadiness is seen to be related to the formation of a vortex near the junction of upper shear layer and the termination point of the supersonic jet, its breakdown, and then its propagation along the upper portion of the cylinder, causing shear layers to be generated and then shed."* The published plots of the peak pressure and the jet impingement angle for a particular configuration show a quite regular pattern with only minor variations in the magnitude over a longer period of time. This is in contrast to results of a slightly modified configuration with a lower angle of the oblique shock wave and a higher impingement location on the bow shock. In this case, only initial oscillations were discovered. These were strongly damped in time and resulted into a steady-state solution. This effect was also supported by a coarser grid resolution.

Furumoto *et al.* (1996) also observed the unsteady characteristics of the Edney type IV interaction in their simulations of 5-species air in thermochemical nonequilibrium. The investigated configuration resulted in stronger unsteady characteristics in the initial phase of the simulation. A sustained oscillation in the maximum surface pressure could be reached once all transients of the solution were damped out. Furumoto et al. concluded that the most stable solution was obtained with a shock impingement angle which leads to a shock-shock interaction in the transition regime between a type III and IV interaction. In case of more unstable solutions, *"the largest degree of unsteadiness was the result of alternating shed vortices both above and below the jet"* (Furumoto *et al.* (1996)) which is similar to the mechanism described by Lind & Lewis (1996), though the vortex shedding on both sides of the jet seems to be influential in the configuration of Furumoto et al. Observations of unsteady behaviour with different intensities are also reported by several other authors, for example Yamamoto *et al.* (1999) and Gaitonde (1993).

Sanderson *et al.* (2004) experimentally investigated the influence of nonequilibrium dissociation on the Edney type IV shock-shock interaction. The aim of the experimental study was to investigate the effects of high enthalpy thermochemistry on the Edney type IV interaction. Sanderson (1995) encountered oscillation frequencies from $5 - 15\,kHz$ in the experimental investigations of a low enthalpy test case from a series of three different enthalpy configurations. The quality of the frequency spectra of the other test cases was limited due to the small number of observed cycles. The Strouhal number, $Sh = fD/u_\infty$, was estimated for the intermediate enthalpy test case B as $0.11 \pm 100\%$. Plotted data of the experimental campaign are available in a frequency range of 10^3 to $10^5\,Hz$. The data was recorded at a sampling rate of $200\,kHz$.

3. Computational Setup

The unsteady Edney type IV and type VII shock-shock interactions are investigated by means of a CFD analysis. The physical models applied in the simulation as well as

the numerical methods are described in Sections 3.1 and 3.2. Section 3.3 addresses the grid quality, followed by a discussion of the applied boundary conditions in Section 3.4. The configuration of the grid adaptation is described in Section 3.5. A more detailed discussion of the computational setup is given in Windisch (2014) and in the respective references of the models.

3.1. *Physical modelling*

3.1.1. *Flow equations*

The mixture of thermally perfect gases is governed by the Navier-Stokes equations, which are extended to account for partial densities of single species and a combined internal energy mode of all molecules. The system is solved for all but one partial densities, as the density of the remaining species may be computed from the global density.

For closure, the pressure is modelled as a mixture of perfect gases via the equation of state. All required quantities of the gas mixture are weighted by the mass fractions of the corresponding species.

3.1.2. *Nonequilibrium models*

The chemical nonequilibrium source term is computed by a finite rate chemistry model (Anderson (1989)). The forward reaction rates are described by the modified Arrhenius equation. The backward reaction rates are computed from the equilibrium constants, which are computed from tabulated data (Stull & Prophet (2011)).

For the simulation of nitrogen flow, the Park 85 reaction rate model (Park (1985)) is applied. Atomic and molecular nitrogen is considered here. The Martian atmosphere is simulated by application of the Park CO_2 reaction rate model (Park *et al.* (1994)). The system considers a total of 12 species: Ar, C, N, O, C_2, O_2, CN, CO, NO, CO_2, NCO, and N_2.

A two-temperature model is applied, as thermochemical nonequilibrium simulations of flows which consider the Martian atmosphere are frequently found to deviate only slightly from the thermal equilibrium state (Wright *et al.* (2010)), even for reentry configurations. The electronic energy modes of molecular species and the vibrational energy modes are combined in a single vibrational temperature. The two-temperature model is also the natural choice for the two-species nitrogen model with only one molecular species.

The thermal source term can be split into the vibration-dissociation coupling and the vibrational-translational energy exchange. The vibration-dissociation coupling is modelled via the Park average temperature model (Anderson (1989)). All reactions are considered for the vibrational energy coupling. The Millikan and White model (Millikan & White (1963)) is applied to capture the vibrational-translational energy exchange. Details on the applied data sets are discussed in Windisch (2014).

3.1.3. *Thermodynamic and transport properties*

To simplify data handling for various reaction models, all data on energies and specific heat capacities are stored as piece-wise polynomials and evaluated as needed. The shear stresses are determined by the usual Newtonian fluid assumption. The diffusion flux is computed by applying a constant Lewis number. The energy transport is driven by two forces, the thermal conduction caused by temperature gradients and the transport of enthalpy driven by diffusion. The thermal conductivity is computed assuming a constant Prandtl number.

In case of pure nitrogen flow (N_2), the viscosity is calculated via Sutherland's law. A constant Prandtl number $Pr = 0.7$ and a constant Lewis number $Le = 1.0$ are applied.

The curve fits for the thermodynamic properties are based on statistical thermodynamics (Anderson (1989)).

In case of the Park CO_2 reaction model, the species' viscosities are calculated via curve fits based on the Chapman-Enskog theory (Bird *et al.* (2007)). Wilke's semi-empirical mixing-rule is applied to compute the overall gas mixture viscosity. A constant Prandtl number approximated as $Pr = 0.74$ is applied for the calculation of the gas mixture conductivity. A Lewis number of $Le = 0.6$ is taken into account. The thermodynamic properties are calculated with tabulated data by Capitelli *et al.* (2005*a*,*b*).

3.2. *Numerical methods*

The scientific code QUADFLOW (Bramkamp *et al.* (2004)) solves the Navier-Stokes equations around complex aerodynamic configurations by a cell-centred finite volume method on locally refined grids. The convective fluxes are determined by solving quasi-one-dimensional Riemann problems at the cell interfaces. For the investigated configuration, the AUSM upwind method is found to deliver accurate results at high grid resolutions with no tendency for carbuncle phenomena. A linear, multidimensional Green-Gauss reconstruction of the transported variables is applied to increase the spatial accuracy. In order to avoid oscillations in the vicinity of local extrema and discontinuities, a Venkatakrishnan limiter with TVD property is used. Concerning the computation of the viscous fluxes, the gradients of the variables at cell interfaces are determined using the divergence theorem. A second order approximation of the wall temperature gradient is applied to enhance the resolution of the wall heat flux.

Grid adaptation is based on multiscale analysis instead of classical gradient- or residual-based error estimators, cf. Müller (2003). This adaptation procedure, which is based on data compression strategies from image processing, is the key to sufficiently resolving all relevant flow features. The cell averages on a given level of resolution are represented as cell averages on some coarse level, where the fine scale information is encoded in arrays of detail coefficients of ascending resolution. This requires a hierarchy of nested grids of increasing resolution. The multiscale analysis is used to create locally refined grids. The idea is simply to discard all detail coefficients whose absolute value fall below a certain level-dependent threshold, which means that the grid is locally coarsened in this area. Computations are usually started on level $L = 1$, so that the detail coefficients between level $L = 1$ and level $L = 0$ can be used in the adaptation process. In order to obtain the required grid geometry at any given level, a fairly general representation of the grid is required. The computational grids are represented by block-structured parametric B-Spline patches which allow interpolation of geometric data at each location and can deal with complex geometries, cf. Lamby (2007). Details on the applied numerical methods are published in Windisch (2014).

Several constraints have to be taken into account when selecting the time-integration method for the current test configuration. An explicit method would be a common choice for unsteady flow fields. However, the high stiffness of the thermochemical nonequilibrium source term prohibits the use of an explicit method for the present configuration and requires instead the use of an implicit method or the use of an explicit-implicit method. In the latter case, the flow equations are advanced in time with an explicit method while an implicit method is applied to the thermochemical source terms. In either case, the frequent evaluation of the source term Jacobians is quite costly, given the long run-time of the present unsteady simulations. The use of an explicit-implicit method is therefore not a good choice as it would involve high computational costs for the evaluation of the source term Jacobian, but still imposes a significant limitation on the time step, as a Courant-Friedrichs-Lewy (CFL) number below approximately 0.5 needs to be used

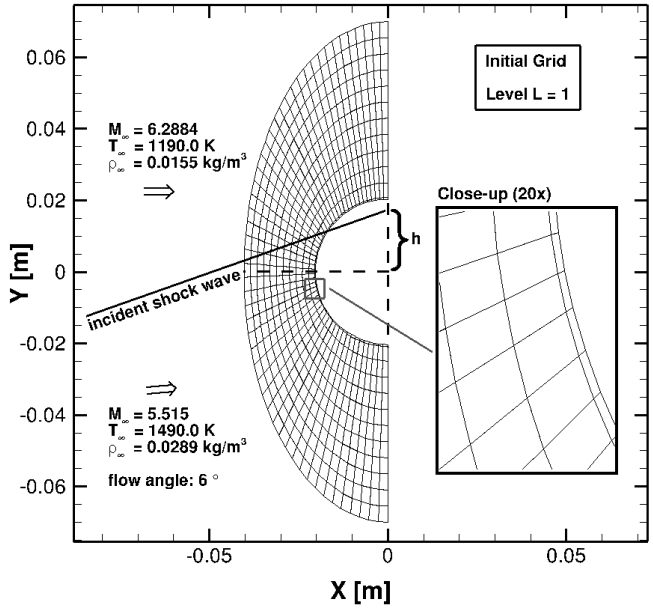

FIGURE 1. Initial grid with high grid stretching and schematic drawing of incident shock wave. Not to scale.

for the explicit-implicit method on higher levels. A remedy to these high costs is the use of an implicit method. The implicit method allows for larger CFL numbers than the explicit-implicit method, which reduces the overall number of iterations required to reach a given point in time. This reduces the number of evaluations of the Jacobians. Several choices exist for the implicit time-integration method. The implicit first-order backward Euler method was selected here, as this method represents a good trade-off concerning efficiency, stability and accuracy for the current configuration. Only one evaluation of the Jacobians is required in each Newton iteration step. The overall computational efficiency increases with the backward Euler method as compared to the use of the explicit-implicit method. The highly resolved grids reduce the numerical dissipation and compensate the low temporal accuracy.

3.3. *Grid geometry and stretching*

A proper design of the grid is crucial for the simulation of the investigated shock-shock interactions. While the grid adaptation concept allows for an automatic detection of the grid areas which need a high grid resolution, the coarse grid discretization must take care of a proper cell geometry to avoid too many refinement levels in the boundary layer. Especially the grid stretching is crucial in the present configuration. On the one hand, a grid converged resolution of the heat flux requires a high stretching of the boundary cells. On the other hand, a uniform grid is advantageous for the resolution of the inner flow field. The transition between both grid stretchings needs to be smooth and adequately located to avoid any numerical instabilities.

An example of the initial grid on level $L = 1$ is shown in figure 1. The grid covers half of the cylinder geometry and has a size of $0.02\,m$ in wall normal direction measured on the symmetry line. The coarse grid discretization consists of 624 cells. A piece-wise defined

	upper	lower
$\rho_\infty\ [kg/m^3]$	0.0155	0.0289
$M_\infty\ [-]$	6.2884	5.515
$T_\infty\ [K]$	1190.0	1490.0

	composition	(lower and upper)		
Nitrogen	$X_{N_2}\ [-]$	$X_N\ [-]$		
	0.99	0.01		
Mars	$X_{Ar}\ [-]$	$X_{CO_2}\ [-]$	$X_{N_2}\ [-]$	$X_{other}\ [-]$
	0.0147	0.9670	0.0174	0.0001

TABLE 1. Inflow conditions.

stretching function is used in wall normal direction. The switching between a logarithmic stretching function and a uniform grid is located at $x = -0.0207\,m$, measured on the symmetry line with the center of the cylinder located in the coordinate system origin. The stretching is designed to lead to a cell height of $1.7 \times 10^{-7}\,m$ directly at the wall on the target grid refinement level. The grid stretching in the present configuration is selected to lead to a maximum aspect ratio of $AR = 200$ on the target grid refinement level.

The uniform grid in the inner flow field is important to properly capture both triple points of the shock-shock interaction. For a uniform grid, a total of ten percent of the grid cells is located in only two percent of the physical domain. This results in a significant increase in the number of grid points close to the wall. The grid lines in circumferential direction are uniformly distributed.

3.4. *Boundary conditions*

The far field boundary of the grid in wall normal direction represents the supersonic inflow boundary. This boundary is split into two parts to simulate the incident oblique shock wave. On the upper part of the inflow boundary, the free-stream flow conditions are used, on the lower part, the flow conditions behind the oblique shock wave are applied as inflow conditions, see table 1. The flow state behind the incident oblique shock wave was computed in a separate simulation of the shock generator in order to get proper inflow conditions for the applied nitrogen reaction model. The inflow conditions correspond to an intermediate enthalpy test configuration in an experimental investigation by Sanderson (1995).

The location of the splitting is defined by the incident shock wave with a 15°-angle and the height h as indicated in figure 1. The value of h is non-dimensionalized by the radius $r = 0.0203\,m$ of the cylinder. Different values of h are selected, as this parameter can be used to control the actual type of the Edney shock-shock interaction. A value of $h = 0.08$ is selected for nitrogen flow in thermochemical nonequilibrium, as this leads to roughly similar locations of the triple points as in the experimental results. The solution is close to an Edney type IVa interaction and shows a pronounced unsteady behaviour. For simulations with the Park CO_2 reaction model in thermochemical nonequilibrium, a value of $h = 0.09$ delivers simulation results which may be characterized as an Edney type VII interaction as defined by Yamamoto *et al.* (1999). It should be noted that in

this case a reduced height of $h = 0.05$ would lead to a shock-shock interaction which is similar to an Edney type IVa interaction (Furumoto *et al.* (1996)) as discussed in Windisch (2014).

A supersonic outflow boundary condition is defined at the upper and lower edges of the grid. Due to the short test time, an isothermal wall at ambient temperature of $300\,K$ is assumed at the surface of the cylinder.

The solution is advanced in time with a global time-stepping to ensure time consistency of the solution. The time steps are small enough to capture and resolve all major unsteady effects of the flow field.

3.5. *Grid adaptation*

The refinement strategy of the multiscale based grid adaptation leads to a refinement of the grid not only in areas which require a high resolution, but also in a small area around these flow features. Since the jet moves only slowly with respect to the applied number of iterations, grid adaptation is not needed after every iteration step. In case of highly-resolved simulations with a target grid level of $L = 8$, grid adaptations are carried out every 100 iterations after reaching the target level. This strategy reflects a good trade-off between the computational effort and the proper resolution of the flow field, as the jet moves only slowly and does not leave the fully refined area within 100 iterations.

4. Nitrogen flow: Edney type IV interaction

The Edney type IV shock-shock interaction is an important configuration in engineering applications. Section 4.1 categorizes the unsteady mechanisms to allow for an easier discussion in the subsequent sections. The unsteady flow features are discussed in Section 4.2, followed by the wall heat flux in Section 4.3. The chapter is concluded in Section 4.4 with a discussion of the grid adaptation and an analysis of the sensitivity of the solution with respect to space and time.

4.1. *Classification of unsteady mechanism*

In order to address the flow field features, the unsteady mechanisms need to be characterized. A schematic drawing of the jet structure is depicted in figure 2. Black solid lines indicate the border between supersonic and subsonic parts of the flow domain. Six main supersonic areas in the flow field, indicated by number $1 - 6$ have been identified. In principal, all unsteady phenomena in the flow field are strongly coupled and depend on each other. However, the subdivision of the flow domain helps to identify six unsteady mechanisms:

(a) The curvature and location of the bow shocks (green arrows) is affected by pressure waves passing through the flow field and by the thickness of zone five.

(b) Zones one to three may rotate (yellow arrows) around the center of the interface between different zones. The rotation is due to the relocation and changes in strength of the compression and expansion pattern.

(c) This effect is coupled to a longitudinal expansion and compression of the zones one to three (blue arrows).

(d) Zone four may emerge in the flow field and eventually integrate into either zone three or zone five. This mechanism supports mechanism (e).

(e) The transition of the Edney type IV interaction into an Edney type IVa interaction (red arrow) in which zones one through five are interconnected in the supersonic jet.

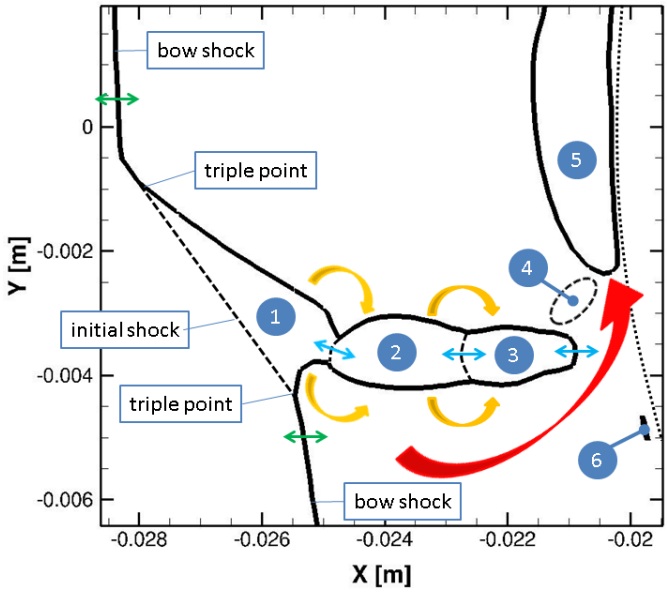

FIGURE 2. Schematic drawing of jet unsteady mechanism. Sonic line indicated in bold black. The numbers mark the six main supersonic flow regions in the vicinity of the jet.

(f) Zones five and six change their size and location, including the distance to the wall.

The preceding characterization is based only on the supersonic jet structure since it can be most easily investigated. Other unsteady phenomena, such as the formation and shedding of vortices and propagating pressure waves may lead to different characterizations. However, the influences of these effects on the jet structure are included in the above analysis and an additional analysis of these flow features would not reveal significant additional insights into the flow problem.

4.2. *Flow field*

4.2.1. *Unsteady mechanism*

In the following, the flow field solution and the jet unsteadiness are discussed in more detail. The analysis is carried out by means of a highly resolved simulation on level $L = 8$ in thermochemical nonequilibrium. After the first performed grid adaptation reaching to level $L = 8$, this instant in time is defined as the reference time $t = 0\ s$. All major characteristic unsteady phenomena as indicated in figure 2 can be identified in the solution.

The unsteady mechanism (e) is the most dominant flow feature, see figure 3: The unsteady cycle starts with the lower turning point at time $t = 1.026 \times 10^{-6}\ s$. This does not coincide with time $t = 0\ s$, as the jet is moving upward and downward when reaching level $L = 8$ for the first time, compare $t = 0.639 \times 10^{-6}\ s$ and $t = 1.026 \times 10^{-6}\ s$. The solution cycle ends at time $t = 5.151 \times 10^{-6}\ s$ which leads to a time period of $t = 4.13 \times 10^{-6}\ s$ or a frequency of approximately $242\ kHz$.

The jet is moving upwards at the beginning of the solution cycle of mechanism (e) at $t = 1.026 \times 10^{-6}\ s$. When reaching the upper turning point at $t = 2.677 \times 10^{-6}\ s$, zones two, three and five are interconnected to a single supersonic jet. The jet is then moving downward, increasing the distance to zone five and building up a subsonic part in between the zones, compare $t = 3.393 \times 10^{-6}\ s$. Mechanism ($d$) results from a contraction

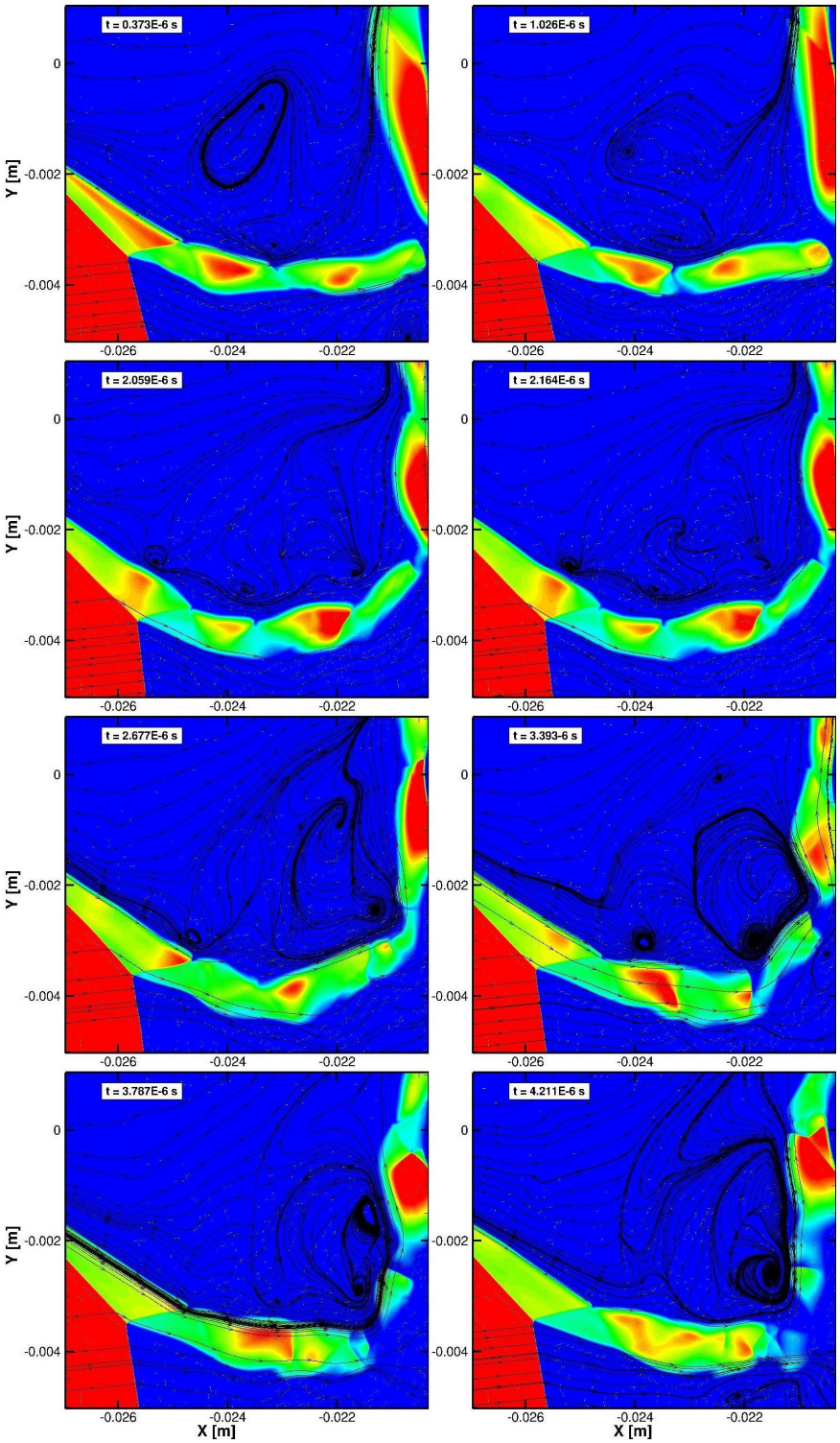

FIGURE 3. Formation and shedding of vortices. Jet structure indicated by Mach number contour plot with restricted range $M = 1 \ldots 2$.

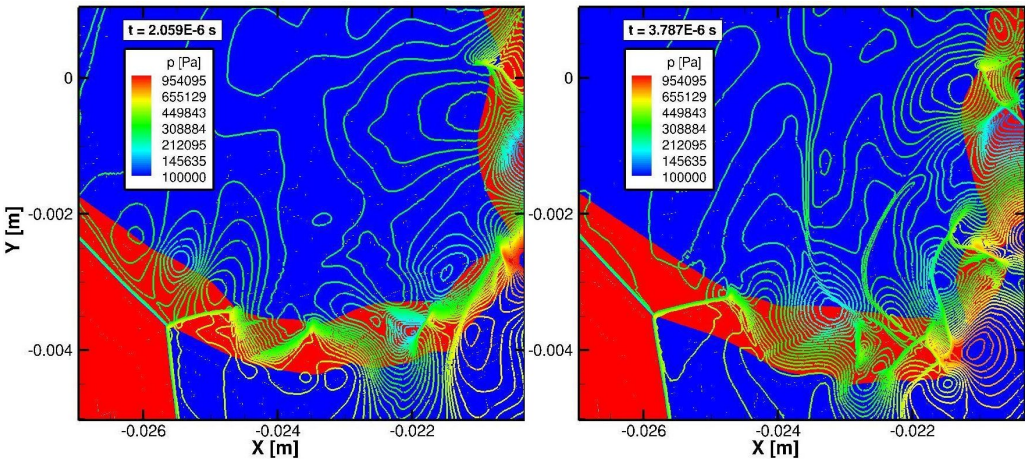

FIGURE 4. Isolines of pressure waves. Jet shape indicated by transition between supersonic (red) and subsonic (blue) flow.

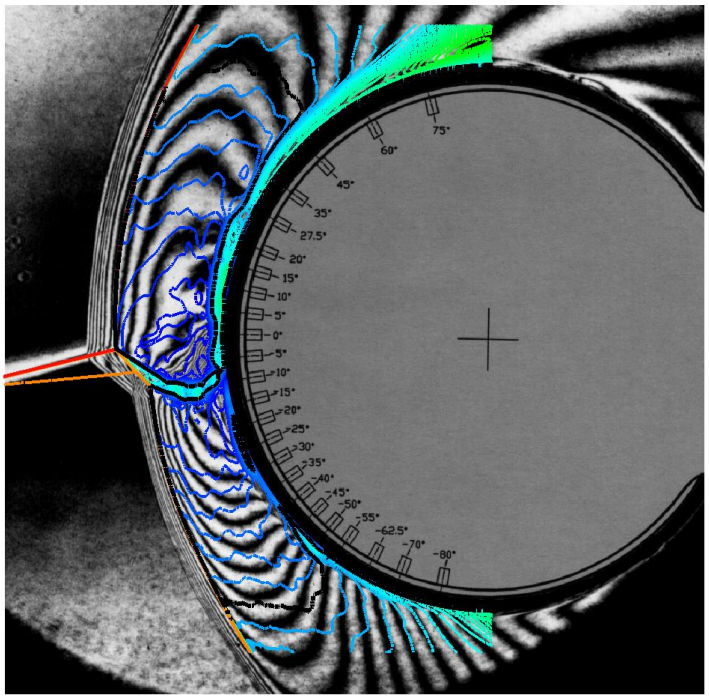

FIGURE 5. Comparison of the Mach number isolines at time $3.210 \times 10^{-6}\,s$ with the experimental fringes of the flow field. Sonic line indicated by black line. Picture taken by Sanderson (1995).

of the jet end which finally leads to the supersonic zone four, $t = 3.787 \times 10^{-6}\ s$. As mechanism (f) changes the size of zone five, zones four and five eventually connect at time $t = 4.211 \times 10^{-6} s$. The main unsteady mechanism (e) starts over again after finishing the main downward motion of the jet zones two and three by movements with smaller amplitude.

Mechanisms (b) and (c), i.e., rotations of zones one to three and a longitudinal expansion and compression of the jet, can be observed throughout the whole solution cycle.

Both are major driving mechanisms for the unsteady movement (e). The amplitude of mechanism (a) is rather small on higher grid levels. It can best be identified in figure 3 when comparing the intersection of the sonic line with the x-axis, for instance at times $t = 1.026 \times 10^{-6}\ s$ and $t = 3.787 \times 10^{-6}\ s$.

The frequency range of the unsteady phenomena depends strongly on the specific configuration under consideration, in particular on the location of the impinging shock wave. Compared to the experiment, the numerical simulation is capable of resolving a much higher frequency range of the physical instabilities as a time step size of approximately $\approx 1.3 \times 10^{-10}\ s$ is applied. The frequency of the main identified unsteady mechanism is about one order of magnitude larger than the frequencies measured in the experimental campaign.

The discussion in Section 2 indicates that various authors found a relation between the jet unsteadiness and the formation and shedding of vortices. This general finding is confirmed in the present study, though the detailed mechanism seems to be different.

During the solution cycle, up to five vortices are generated in the flow domain above the supersonic jet at $t = 2.164 \times 10^{-6}\ s$, see Figure 3, while at most two vortices are found in the area below the jet. The observation of shed vortices on both sides of the supersonic jet is in agreement to the findings by Furumoto *et al.* (1996). However, in the present study the vortices above the supersonic jet are strongly related to the jet movement while the main vortex below the jet is more steady and seems to be only of minor importance. The vortex below the jet is located at a larger distance to the jet and exists longer than the vortices above the jet.

The observed coupling of the vortices above the jet to the jet unsteadiness is to some extent in agreement with the results by Lind & Lewis (1996). They identified a coupling between a vortex in the upper shear layer and the high-frequency jet unsteadiness. The formation of a single vortex was observed *"near the junction of upper shear layer and the termination point of the supersonic jet"*. In the present work, the formation and shedding of several vortices is more pronounced near the junctions between the jet zones two, three and four as defined in figure 2. This includes two strong vortices near the jet termination point at time $t = 3.787 \times 10^{-6}\ s$, see figure 3.

In the simulations by Lind and Lewis the generated vortex propagates along the upper portion of the cylinder and is related to the main pressure cycle. Such a transport of vortices over a larger part of the flow domain could not be observed in the present study. Instead, vortices are formed and dissipated several times during each time period of the main unsteady mechanism (e). An example of this frequent and rapid development of the flow field is given in figure 3, compare for instance solution time $t = 2.059 \times 10^{-6}\ s$ with $t = 2.164 \times 10^{-6}\ s$. Within only a short period of time, a new vortex is formed in the middle of the flow field while the upper middle vortex moved to the left and became much stronger. At solution times when the jet structure is close to an Edney type III interaction, the formation and dissipation of vortices is more pronounced in the inner part of the flow field and above the supersonic jet, i.e., zones two and three. At solutions times when zone four is present, the formation and shedding of vortices is more pronounced in this part of the flow domain.

In general, the formation, dissipation and shedding of vortices is coupled to pressure waves which are propagating at high speeds from right to left through the subsonic part of the flow domain. Figure 4 illustrates that pressure waves exist in the entire flow field.

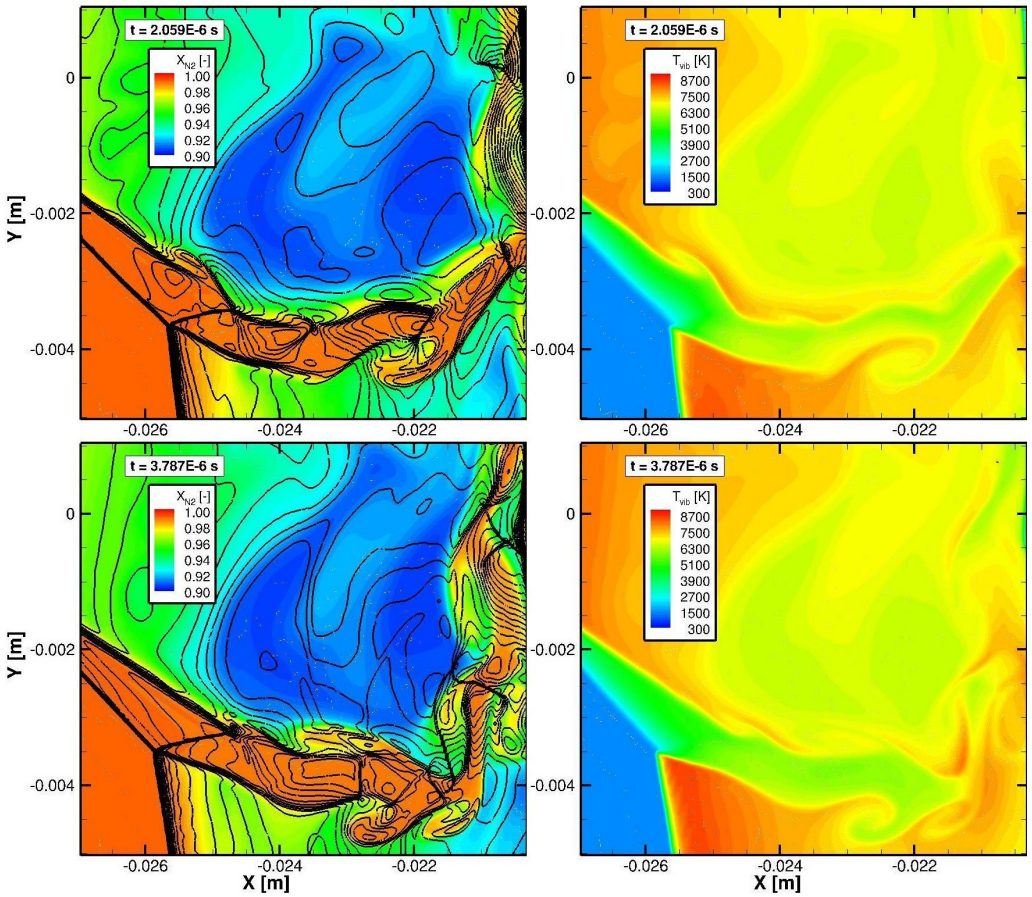

FIGURE 6. Contour plot of N_2 mass fractions (left) and vibrational temperature (right). Isolines of translational temperature (left).

The structure of the pressure field is strongly coupled to the formation of vortices and the wave patterns inside the supersonic jet. After an initial oblique shock wave the flow inside the jet is redirected through a series of expansion and compression waves. The location and the type (compression, expansion) of these wave patterns change with time as indicated by the local Mach number in figure 3 and the pressure contours in figure 4.

A strong compression wave which is almost normal to the flow direction can be observed at time $t = 3.787 \times 10^{-6}$ s. This flow feature emerges from the alternating compression-expansion wave pattern and belongs to a part of the jet where all wave patterns are highly unsteady. The flow remains supersonic while passing through this compression and is again accelerated further downstream. At the end of the supersonic jet, the expansion and compression wave patterns tend to become more symmetric with respect to the jet center. The jet curvature becomes so strong, that the compression of the flow leads to a subsonic part which separates zones three and four, see figure 3.

4.2.2. *Nonequilibrium effects*

Figure 6 illustrates the dissociation of molecular nitrogen in the flow field. Through the vibration-dissociation coupling, the chemical reactions are closely tied to the translational

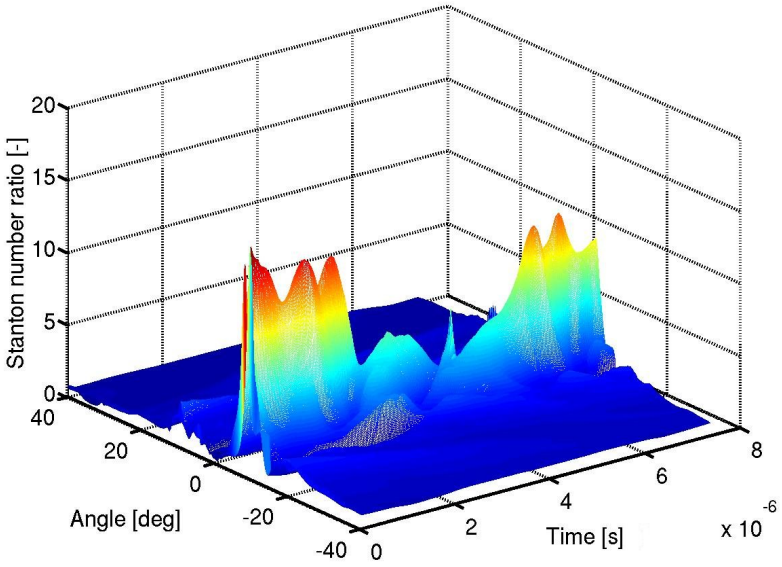

FIGURE 7. Stanton number distribution over time for the flow field illustrated in figure 3.

and vibrational temperature. Only moderate delays in the excitation of the vibrational energy mode by the vibrational-translational energy can be observed, most notably in the shock zone after the bow shocks. The oblique shock wave in front of the supersonic jet, which connects both triple points, and the following pattern of oblique shock waves is much weaker than the upper and lower bow shock. The vibrational temperature remains almost constant in the main core of the supersonic jet. Comparing figures 4 and 6 indicates similarities in the pressure distribution and the vibrational temperature of the flow field. On the one hand, higher pressures reduce the relaxation time of the vibrational-energy exchange which increases the amount of vibrational energy. On the other hand, a higher pressure leads to stronger dissociations along with a depletion of vibrational energy. The latter effect is more pronounced in the vicinity of the sonic lines. The depletion of vibrational energy is supported by mixing processes and energy exchanges through conduction and diffusion. For clarification it should be noted here that in general both, chemical reactions as well as the vibrational-translational energy exchange are coupled to the flow field with a certain delay. This gives time for convective transport which has a significant influence on the flow field.

4.3. *Wall Quantities*

Figure 7 depicts the development of the Stanton number ratio over time. The Stanton number is normalized by the theoretical value for the stagnation point flow according to Fay & Riddell (1958), $St_{Fay\&Riddell} = 0.0172$. The angle is measured from the geometric stagnation point, i.e., the center line of the cylinder.

Strong peaks are located at the jet end. All significant unsteady changes of the heat flux take place at a range between $-20.0°$ and $+20.0°$ with respect to the geometric stagnation point.

The Stanton number distribution for one cycle of the unsteady mechanism (e) from $t = 1.026 \times 10^{-6}\ s$ to $t = 5.151 \times 10^{-6}\ s$ is plotted in figure 8. A data set is written

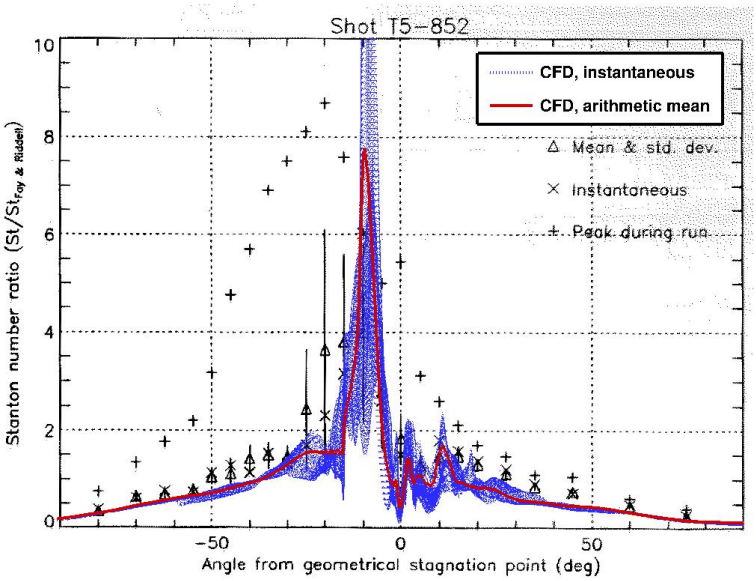

FIGURE 8. Stanton number distribution at the wall for one full cycle of the unsteady mechanism. Output written approximately every 1.3×10^{-8} s. Comparison with experimental data from Sanderson (1995).

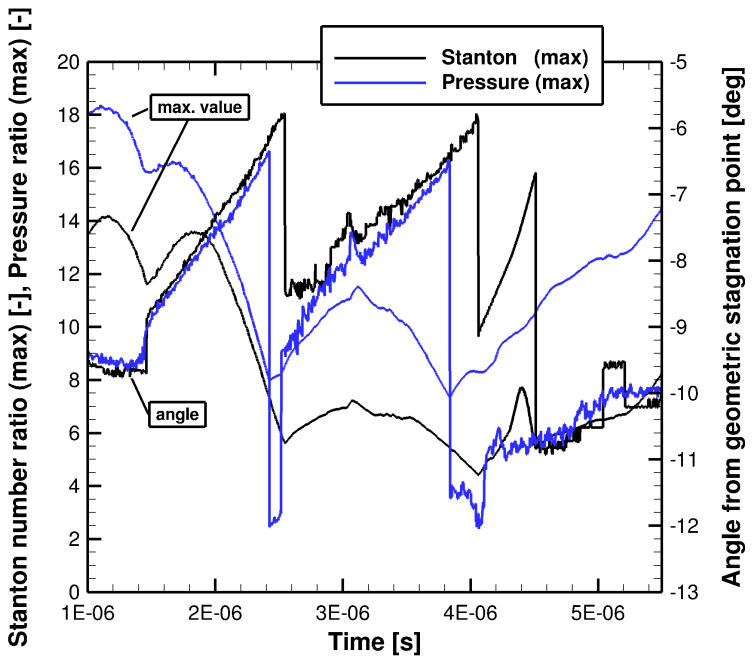

FIGURE 9. Oscillations of maximum Stanton number and maximum pressure for the flow field illustrated in figure 3.

approximately every 1.3×10^{-8} s and depicted with dotted lines. The point density in this plot is a measure for the accumulated duration of the corresponding value.

The computed heat flux rates as well as the calculated arithmetic means are in good agreement with the experimental measurements by Sanderson (1995). The experimental results indicate larger standard deviations in the area where the main unsteady fluctuations were found in the simulation. The present results support the unsteady behavior of the heat flux found by Sanderson (1995). The duration of one cycle of the unsteady mechanism is small. Hence, the arithmetic mean of the Stanton number ratio is a good measure for the expected heat load in engineering applications. This value corresponds to a time weighted average, as the time step size remains similar during the whole computation.

An analysis of the maximum ratio for pressure and the Stanton number reveals more insight into the coupling with the unsteady mechanism. The characteristics of the jet movement, compare for example figure 3, are well reflected in the wall quantities.

The maximum Stanton number ratio of approximately 14.2 can be found at $t \approx 1.15 \times 10^{-6}$ s when the jet impinges almost horizontally on the cylinder surface. In this case, the Mach disc of the terminating shock wave is almost parallel to the wall surface, with the lower corner being a bit closer to the wall. This changes at $t \approx 1.45 \times 10^{-6}$ s when the upper corner of the jet end is slightly closer to the wall. An almost discontinuous change of the maximum Stanton number can be observed in figure 9. Subsequently the angle increases as the jet bends upwards. The jet end is now moving further away from the cylinder surface which lowers the wall heat flux at an almost constant rate. At some instant in time the jet gets connected to zone five as illustrated in figure 4 and stops bending further upwards. Instead, zone four tends to move closer to the wall. At about $t \approx 2.54 \times 10^{-6}$ s, the location of the maximum Stanton number ratio switches from the upper end of zone four to the jet side, which is now located closer to the wall. When the jet is moving downwards, zone four separates first from zone five and afterwards from zone three as discussed in Section 4.2. After separating form zone five, zone four keeps on moving upwards which causes again an increase in the angle and the maximum Stanton number ratio. Once zone four has connected to zone five, both supersonic zones move closer to the wall. This causes again a jump in the location of the maximum Stanton number ratio at about $t \approx 4.05 \times 10^{-6}$ s. As the jet end is moving towards the cylinder surface at the same time, the heat flux in this part of the flow domain becomes more prominent again at about $t \approx 4.50 \times 10^{-6}$ s. The cycle ends at $t = 5.151 \times 10^{-6}$ s.

The maximum pressure and the maximum Stanton number ratio are closely coupled and show similar characteristics, even though the pressure is sometimes ahead of the heat flux distribution. Overall, both quantities are mostly affected by the distance of the supersonic zones to the cylinder surface. The location and, to a minor extent, the maximum values are in addition superimposed by high frequency oscillations with a low amplitude. This effect might be coupled to pressure waves traveling through the flow domain.

As the whole unsteady mechanism is very sensitive and to a certain extent overlayed with random numerical and physical noise, the unsteady mechanism is not exactly repeated in successive cycles. This is why the location and magnitude of the Stanton number ratios is not exactly matched at the beginning and the end of the jet. However, the general trend of increasing heat flux and pressure is matched.

configuration	stretching parameter	L	CFL	$\triangle t$ $[s]$
$L8-impl$	2×10^{-4}	8	5.0	$(\approx 1.3 \times 10^{-10})$
$L6-impl$	4×10^{-6}	6	(≈ 4.2)	2.5×10^{-10}
$L5-impl$	4×10^{-6}	5	(≈ 5.6)	1.0×10^{-9}
$L4-impl$	4×10^{-6}	4	(≈ 21.0)	1.0×10^{-8}
$L4-expl$	4×10^{-6}	4	(≈ 1.0)	5.0×10^{-10}

TABLE 2. Computational setting.

4.4. *Sensitivity with respect to space and time discretization*

The effects of the space and time discretization on the unsteady solution have gained only little attention in past publications. The unsteady jet mechanisms are highly sensitive towards even small perturbations in the flow field. A classical grid convergence analysis is not feasible at affordable costs. Any change in the grid resolution will trigger small changes in the flow field, which will result into a slightly different unsteady mechanism. However, the multiresolution approach of the present work allows to analyze the spatial sensitivity. The aim is to analyze the development of the jet unsteady mechanisms on various grid levels. To demonstrate the importance of this topic, the discussion of the grid sensitivity is opened by a warning, on how numerical settings, such as a local limiter freezing, could easily produce misleading solutions.

Given the unsteady flow features of shock-shock interactions, a suitable means to assess grid sensitivities cannot be easily found. If at all, publications in the literature only address the grid convergence of steady state solutions by comparison of solutions on different grids. This procedure was also carried out in one of our previous works, cf. Windisch *et al.* (2012), in which we simulated the present test case using a local limiter freezing. The limiter freezing reduces the spatial order of the numerical scheme in the vicinity of strong shock waves from 2nd to 1st order. This freezes the location of the bow shocks along with any unsteady movement, which in turn leads to a jet structure which is close to steady-state. It is possible to obtain grid convergence in this case for both, the inner flow field and the wall quantities. The agreement with the instantaneous experimental results is very good, especially regarding the wall heat flux. However, releasing the limiter freezing leads to a fully unsteady solution in this case. Hence, the quasi-steady-state result is a misleading solution which, if physically founded at all, does not reflect more than an instantaneous solution of the flow field based on numerical artifacts. From this study one may draw the conclusion that unsteady effects in shock-shock interactions are very sensitive towards increases in numerical dissipation, even if they are already simulated using very high grid resolutions. This is an important and, on such high grid levels, unexpected finding that should also serve as a warning for others when simulating shock-shock interactions.

The high sensitivity of the unsteady jet structure towards any numerical or physical perturbations, is certainly a major challenge in any sensitivity analysis. In addition, as highly-resolved shock-shock interactions in thermochemical nonequilibrium are difficult to simulate and have high computational demands, using higher grid resolutions in the present work to prove grid convergence by a simple comparison is yet not feasible. However, a comparison of the jet unsteady mechanism on different solution levels seems to be a possible means to discuss grid sensitivities. The grid adaptation concept of the QUADFLOW solver allows for an easy adjustment of the grid resolution and is therefore ideally suited for such an analysis.

configuration	level	time step $[s]$	period (max. deviation) $[s]$	grid cells	no. cycles
$L8 - impl$	8	$\approx 1.3 \times 10^{-10}$	$4.1 \cdot \times 10^{-6}$ (n/a)	$\approx 1,527,600$	1
$L6 - impl$	6	2.5×10^{-10}	4.0×10^{-6} $(+15\%, -18\%)$	$\approx 209,800$	10
$L5 - impl$	5	1.0×10^{-9}	3.9×10^{-6} $(+40\%, -45\%)$	$\approx 70,100$	10
$L4 - impl$	4	1.0×10^{-8}	6.4×10^{-6} $(+20\%, -18\%)$	$\approx 23,300$	10
$L4 - expl$	4	5.0×10^{-10}	6.8×10^{-6} $(+68\%, -30\%)$	$\approx 23,300$	10

TABLE 3. Period of jet main movement(e).

Table 2 lists all investigated resolution levels of the present configuration. The previously discussed results are produced with the highly-resolved configuration $L8 - impl$. Levels four to six use the same initial grid with a higher grid stretching. On level $L = 6$, the same cell height is reached directly at the wall as for the lower stretching grid on target level $L = 8$. Unlike for the highly-resolved simulation with a constant CFL number, a constant time step size is used on level $L = 6$ and lower to simplify the comparison of the results.

The subsequent sections are structured as follows: Section 4.4.1 will give a general overview of the computational grid. The sensitivity of the solution with respect to time is briefly analyzed in Section 4.4.2, followed by a sensitivity analysis with respect to grid resolution in Section 4.4.3.

4.4.1. *Grid adaptation process*

A solution on level $L = 8$ is found to be sufficient to resolve all flow features of the nitrogen flow in thermochemical nonequilibrium. A sequence of the grid adaptation process beginning on the initial level $L = 1$ is depicted in figure 10.

Major unsteady phenomena are encountered in the overall simulation. Carrying out grid adaptations every 100 iterations leads to a good trade-off between computational costs and solution accuracy for the present configuration.

The supersonic jet (zones two and three in figure 2) and the upper supersonic area (zone five) show stronger periodic movements. The ongoing relocation of these flow features results into significant changes to the adapted grid. Figures 11 and 12 show snapshots of the grid on level $L = 8$. Unlike the bow shocks and the two triple points of the shock structure which are almost fixed in their location, the jet structure and the expansion and compression waves inside it are moving with time and the grid changes constantly over time. Especially at the very end of the supersonic jet, major movements of the jet structure can be detected. In addition, the compression and expansion waves inside the jet may vary in size. Transient pressure waves, which are propagating through the flow field from right to left, are also detected and resolved by the grid adaptation and can be identified as single spots which are perpendicular to the supersonic jet.

4.4.2. *Temporal resolution*

The temporal resolution is investigated for nitrogen flow by a comparison of an implicit time-integration method ($L4 - impl$) with an explicit-implicit time-integration method ($L4 - expl$) with a significantly smaller time step. This comparison is carried out on level $L = 4$. The coarser grid level allows for the largest time step of the implicit method and serves as an upper bound. The time for one cycle of the unsteady mechanism (e) does not show any notable changes between both simulations, see table 3. The time period is measured from the instant when the direction of the movement is reversed from a

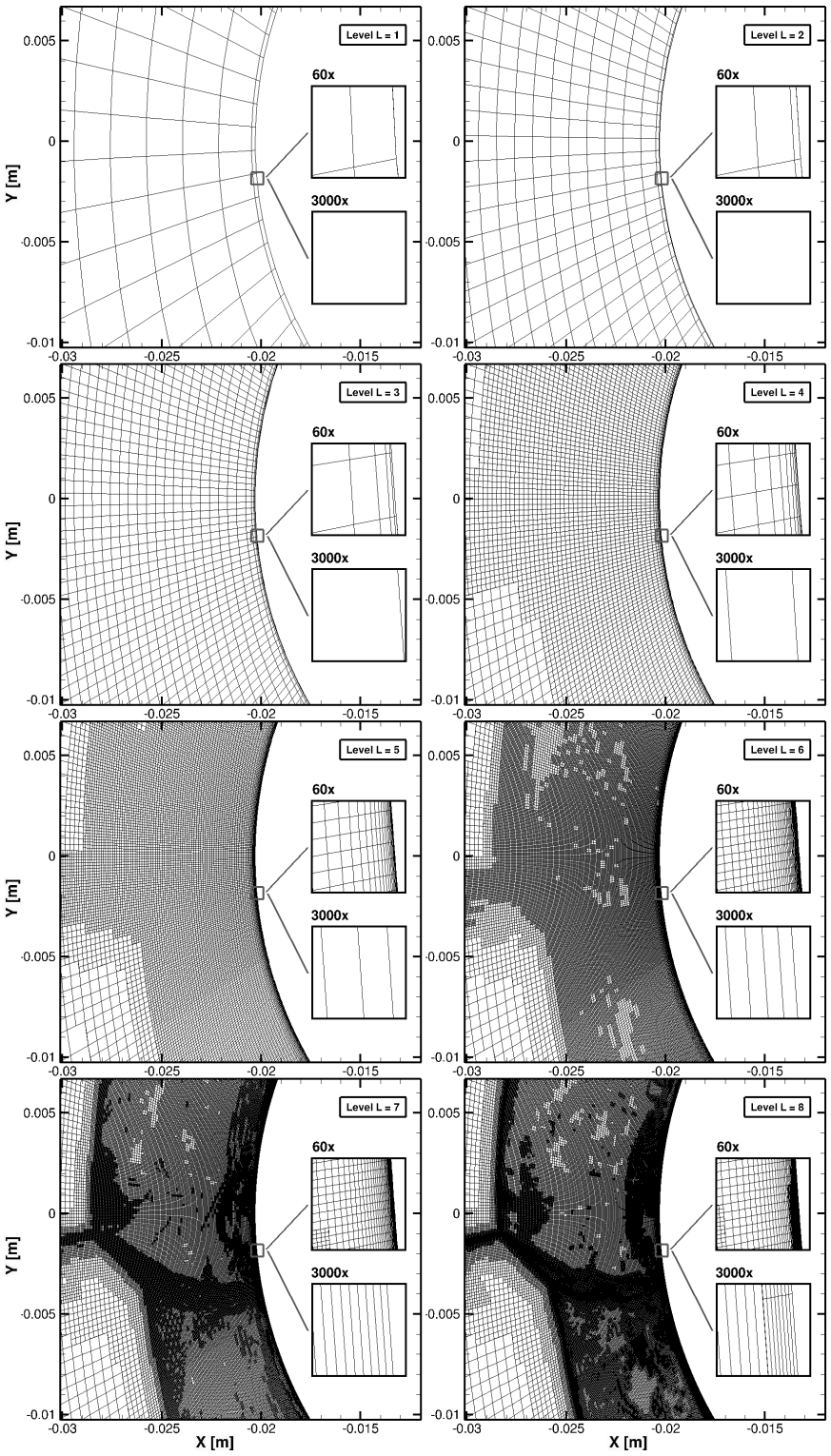

FIGURE 10. Sequence of adapted grids.

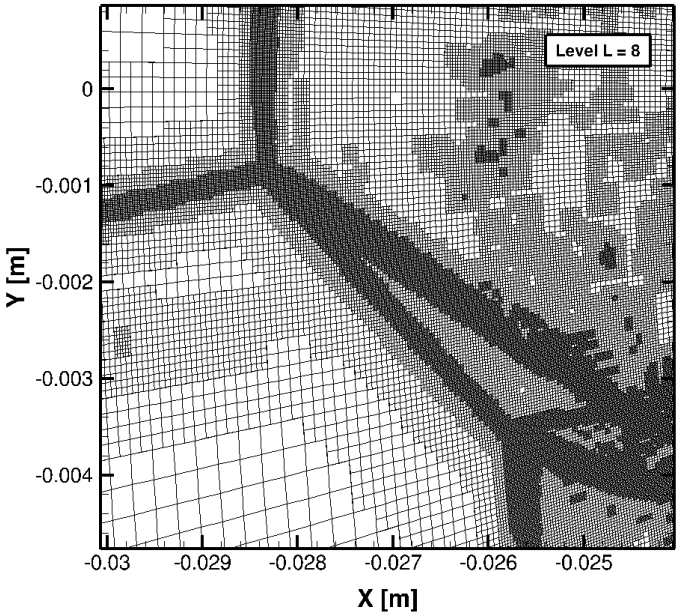

FIGURE 11. Close-up of grid on level $L = 8$ after seven grid adaptations at solution time 3.210×10^{-6} s.

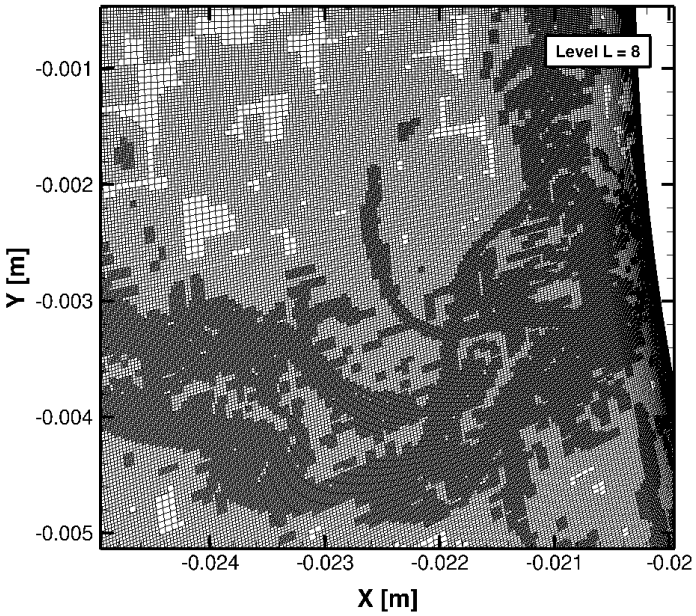

FIGURE 12. Close-up of grid on level $L = 8$ after seven grid adaptations at solution time 3.206×10^{-6} s.

movement away from zone five into a movement towards zone five. This turning point can be described as the state where the shock interaction is closest to an Edney type III interaction. The only minor changes in the average time period of the unsteady mechanism indicate that the implicit method is capable of resolving all major flow features of the unsteady mechanism. This demonstrates that the temporal resolution with a time step as large as $10^{-8}\,s$ is sufficient to capture all physically relevant unsteady mechanism in the flow field. No additional higher frequency movements could be identified in the explicit-implicit flow field solution which could potentially resolve unsteady mechanisms with higher frequencies. In order to compare the time development of the unsteady mechanism over a longer period of time, both solutions are compared for more than 50 cycles of the jet unsteady mechanism. The implicit and explicit solution show similar characteristics. In general, the movement of the unsteady mechanism (e) seems to abate slightly over the course of time until a stable periodic movement with a smaller amplitude is reached. This effect is probably caused by long-term dissipative effects of the flow solver and does not have a notable influence on the time period of the unsteady mechanism. Surprisingly, the unsteady mechanism (a) becomes more pronounced over the course of time. This demonstrates that no low frequency unsteady mechanisms are present in the flow field which could not be resolved in the highly-resolved simulation due to limitations of overall simulated time span.

4.4.3. *Spatial resolution*

The sensitivity of the unsteady mechanism with respect to the spatial resolution is addressed by performing computations on different refinement levels, see table 3. The most pronounced unsteady phenomenon is mechanism (e) which can be identified on all refinement levels. While the highly resolved simulation on level $L = 8$ is computationally most expensive and allows only the computation of one time period, several time periods are simulated on the lower refinement levels. The tabulated time periods represent the arithmetic mean over 10 samples, supplemented by error bounds of the two data samples with the largest deviation. Large variations in the time period of single cycles of the unsteady mechanism can be identified. Measuring the time period is especially difficult on higher levels, on which the generation and the movement of zone four make it difficult to identify the turning points of the movement.

On level $L = 4$ the time for one cycle is significantly larger than for higher refinement levels. In addition, the amplitude of the periodic oscillations tends to become smaller over time. This gradual decay is frequently interrupted by perturbations. The damping of both solutions is a result of the coarser grid resolution which comes along at the expense of a higher dissipation rate. No abatement of the amplitude can be observed on level five or higher, compare the provided video. This underlines the importance of a high grid resolution to properly capture unsteady phenomena. Overall, the discussed phenomena are at least a strong indication for a sufficient resolution of the main unsteady mechanism (e) on levels five or higher, though the uncertainties of the data set are too large to draw any firm conclusions.

Unlike the main unsteady mechanism (e) which is present on all grid levels, the other unsteady mechanisms are stronger affected by the local grid resolution. This will be discussed in the following for the simulations in thermochemical nonequilibrium.

On coarser grid levels the unsteady mechanism (a) leads to stronger deformations of the bow shocks which are traveling in a wave like manner from the triple points to the exterior parts of the bow shock. This is illustrated at several sample times in figure 13 for the configuration ($L4 - impl$), compare $t = 6 \times 10^{-6}\,s$ (red) and $t = 1.09 \times 10^{-5}\,s$ (green). These deformations above and below the incident shock wave can mostly be

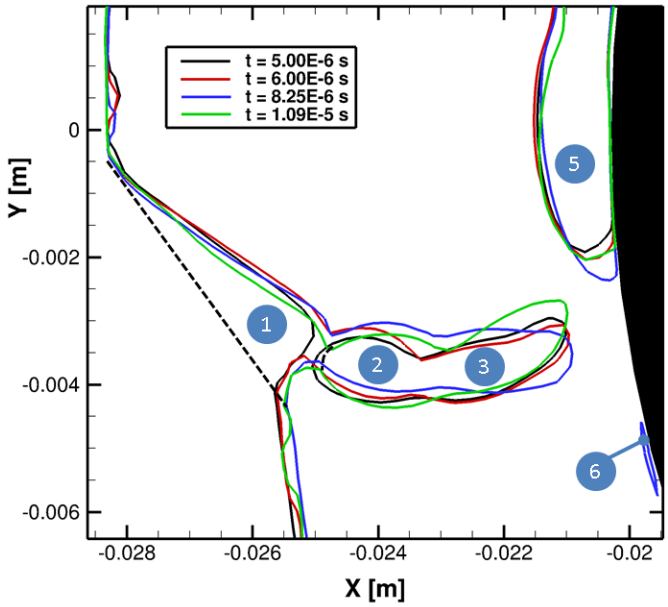

FIGURE 13. Unsteady mechanism (a) on level $L = 4$ ($L4 - impl$). Sonic lines indicated at different times.

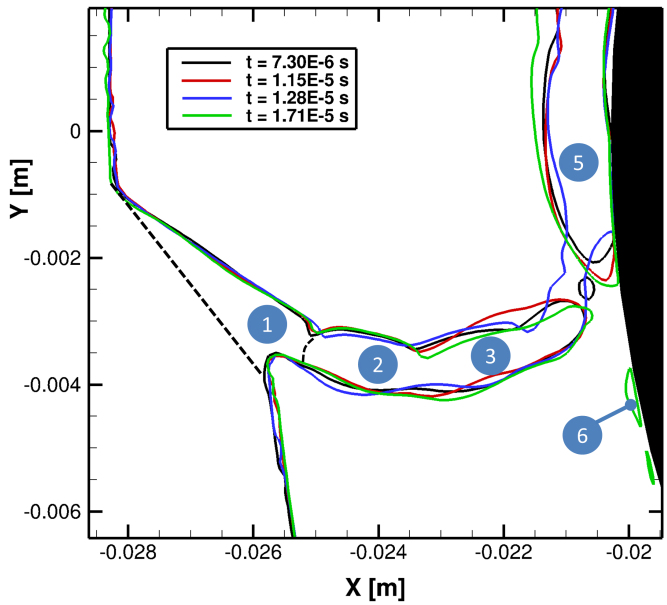

FIGURE 14. Unsteady mechanism (a) on level $L = 5$ ($L5 - impl$). Sonic lines indicated at different times.

observed when the jet end is moving upwards. This effect gets much weaker and better grid converged on finer grid levels, compare figure 14.

The horizontal movements of the shock front as a whole, i.e., changes in the shock stand-off distance, are rather small compared to the jet movement. Surprisingly, the unsteady movement gets more pronounced on higher refinement levels. This indicates that the shock stand-off distance is not coupled to the waves traveling along the shock

front. Instead, this type of unsteadiness is likely to be caused by unsteady movements of zone five on higher grid levels according to mechanism (f). Depending on the actual position, zone five causes a displacement of the subsonic parts of the flow domain which in turn affect the shock stand-off distance. The relocation of zone number five is rather small on level $L = 4$, compare the solution at $t = 8.25 \times 10^{-6}\ s$ (blue) with the other solutions.

The unsteady mechanism (c) is found to be stronger on coarser grid levels. Even a separation between the supersonic zones one and two can be identified on level $L = 4$ at $t = 5 \times 10^{-6} s$ (black). This is likely to be caused by a coarse resolution of the compression and expansion waves which tend to be smeared out on this grid level. The contraction between zones one and two vanishes on higher grid levels where only a small notch-like contraction is left, see for example figures 14 and 3. Small contractions can be found throughout the supersonic jet structure, especially at the end of the jet. On coarser grid levels, zones one through three tend to be smoother, compare figure 13. Mechanism (c) can best be identified comparing the solution at $t = 5 \times 10^{-6} s$ (black) to $t = 1.09 \times 10^{-5} s$ (green).

The unsteady mechanism (d) appears beginning on level $L = 5$ and becomes more significant on higher grid levels. This flow feature seems to be the most grid dependent one of all unsteady mechanisms. The development of this mechanism supports also the unsteady mechanism (e), where zones one through five are interconnected. In addition, the wall distance of the unsteady mechanism (f) becomes larger on higher grid levels.

4.4.4. *Conclusion Sensitivity Analysis*

It may be concluded for the sensitivity analysis that the differences between the flow field solutions on level $L = 5$ ($L5 - impl$) and $L = 6$ ($L6 - impl$) with respect to the main jet unsteady mechanism (e) are small and a good indication of a proper resolution. To be on the safe side, a security margin of two grid adaptations was added to the final test configuration which is carried out on refinement level $L = 8$. This grid was used for all physical analyses of the present work. It consists of approximately 1.5 million cells which is only about 14.9 percent of the number of grid cells of a uniform grid on this level and allows for a high resolution while keeping the computational costs acceptable.

5. Martian atmosphere: Edney type VII interaction

The previous simulations are repeated with $h = 0.09$ utilizing the gas composition of the Martian atmosphere. The resulting flow field is similar to an Edney type VII interaction as defined by Yamamoto *et al.* (1999) for nitrogen flow. For this or similar configurations, no experimental results are known to the author which could be used for comparison.

The main purpose of this test case is to provide new insight into the less known Edney type VII shock-shock interaction and to demonstrate that this kind of shock-shock interaction can also be observed for CO_2 gas compositions.

5.1. *Flow field*

Figure 15 gives an overview of the jet structure at different times. The flow field clearly meets the definition of an Edney type VII interaction by Yamamoto *et al.* (1999). The *"supersonic jet streaming toward the upper downstream without stagnating on the body"* was identified in a simulation of nitrogen flow in thermochemical nonequilibrium for larger values of the impingement shock location h. Unlike for the previous configuration where an Edney type VII configuration could not be generated by increasing the shock

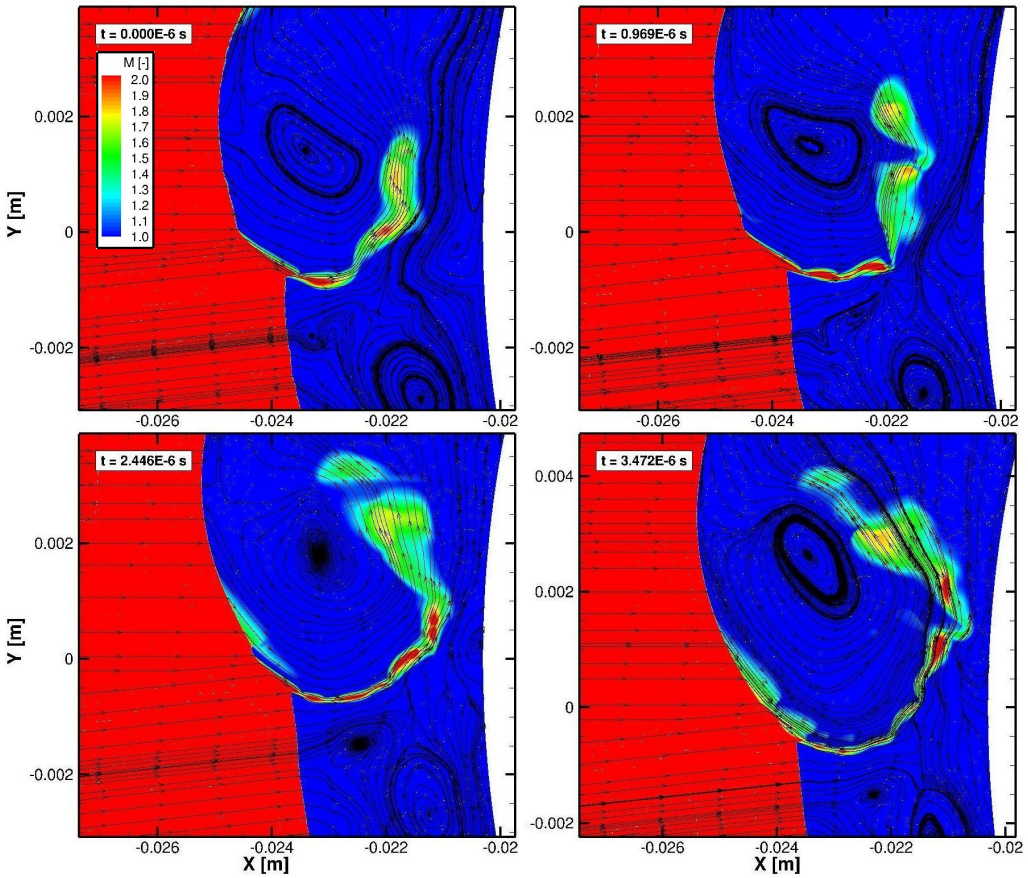

FIGURE 15. Formation and shedding of vortices. Jet structure indicated by Mach number contour plot with restricted range $M = 1 \ldots 2$.

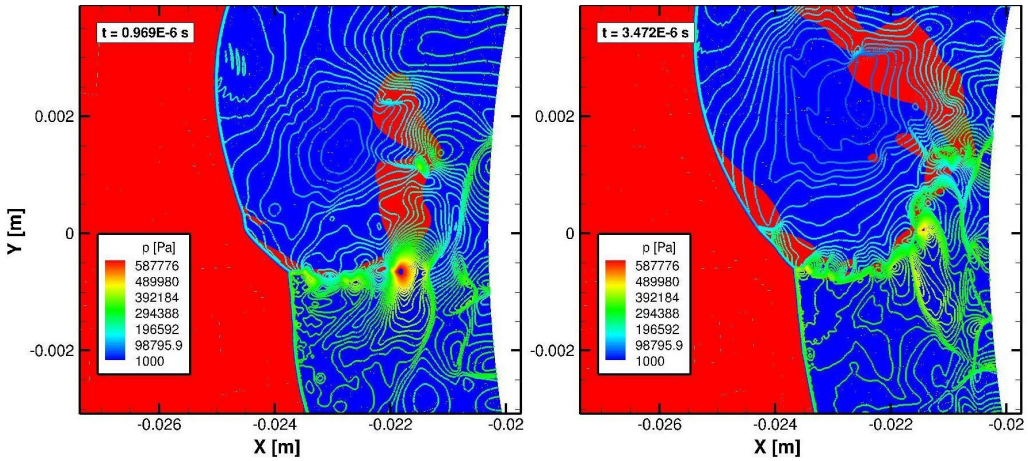

FIGURE 16. Isolines of pressure waves. Jet shape indicated by transition between supersonic (red) and subsonic (blue) flow.

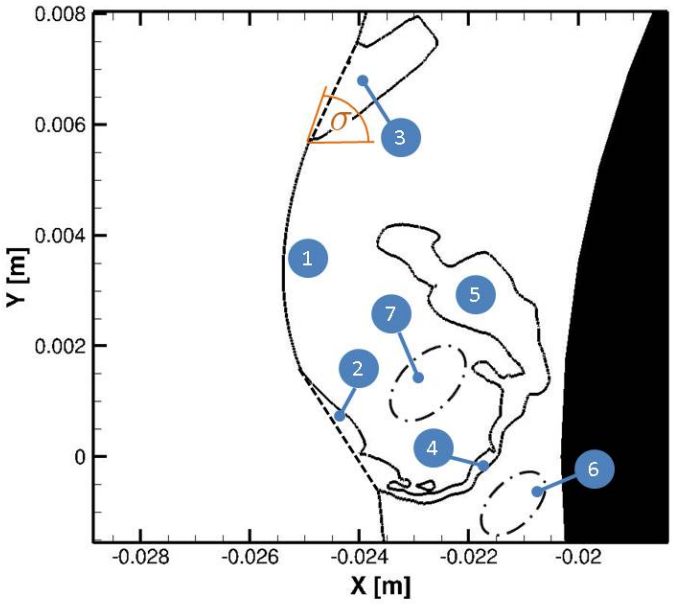

FIGURE 17. Schematic drawing of jet structure. Sonic Line indicated in bold black.

impingement location, the simulation with the Martian atmosphere gas model results into an Edney type VII interaction for a wide range of different impingement locations. The lower bound of the impingement location can be identified as $h = 0.05$ for the present configuration. In this case the Edney type VII interaction is close to an Edney type IVa interaction as discussed by Windisch (2014). However, the flow field is still characterized by a strong vorticity, which is typical of Edney type VII interactions.

5.1.1. *Flow field characteristics*

The main flow features of the present shock-shock interaction are illustrated in figure 17. Zone one comprises the shock layer directly behind the bow shock which is characterized by high translational and vibrational temperatures and the corresponding chemical and thermal relaxation processes. Yamamoto *et al.* (1999) identified this part of the flow domain as the most reactive zone in their nitrogen flow simulations. This finding is qualitatively similar to the CO_2 dominated flow field in the present configuration. A transition from a strong oblique shock wave into a weak oblique shock wave can be found at the boundaries of zones two and three. Assuming a constant isentropic exponent $\gamma = 1.403$, gas dynamic relations for ideal gases from standard text books deliver an angle of $\sigma = 66.6°$ between the local shock front and the inflow direction. This value is reproduced at the lower corner of zone three, while a larger angle is found at the upper corner of zone two. The latter is due to influences of the upper triple point.

Above (zone three) and below (zone two) the upper triple point the flow remains supersonic after passing a weak oblique shock wave. A strong oblique shock wave is formed at the end of zone three. This is a result of the released blockage of the inner flow field once the flow passed the supersonic zone five and zone seven with its high vorticity.

	Nitrogen	CO_2
c_∞ $[m/s]$	707.7	565.1
R $[J/kg \cdot K]$	299.9	191.3
γ $[-]$	1.403	1.403
c_V $[J/kg \cdot K]$	743.8	475.1

TABLE 4. Comparison of gas properties at inflow condition 1.

The inner flow field requires less space after passing these zones and the angle σ gets larger.

The supersonic jet in zone four has similarities to the jet in case of the Edney type IV interaction. Likewise, it consists of two triple points which are almost fixed in space and connect the initial bow shock, an oblique shock wave and a series of alternating compression and expansion waves within the jet structure. Less compression and expansion waves are found in zone five. As pressure and temperature changes become less pronounced in this area. Fewer but still significant chemical reactions are observed in this zone. This opposes the finding by Yamamoto et al. who observed a frozen flow in this area. The discrepancy is likely to be caused by the higher dissociation temperature of molecular nitrogen compared to molecular oxygen and carbon dioxide.

Zones six and seven are characterized by a strong vorticity. Both zones consist of at least one large vortex. Yamamoto et al. found that the flow characteristics in zone six are simpler than in zone seven. This cannot be confirmed in the present configuration. While zone six does not contain the jet structure, more vortices may be present in this zone resulting into a complex flow field with high shear stresses. In agreement to the findings by Yamamoto et al., the pressure in zone six is higher than in zones four, five and seven and causes the jet to bend upwards.

5.1.2. *Nonequilibrium effects*

The shock stand-off distance is significantly reduced for the gas model of the Martian atmosphere. Table 4 tabulates characteristic gas properties for the upper inflow condition and compares these with the gas properties of the nitrogen flow configuration. The lower post-shock temperatures in the current configuration leads to a higher density of the fluid. In addition, the speed of sound is lower in the Martian atmosphere. At a given Mach number, this results into a lower mass flow rate. Combined with the higher density, a much smaller distance between the bow shock and the cylinder wall is sufficient in the present configuration to jettison the entire incoming mass flow.

The vibrational temperature is found to follow closely the translational temperature, except for a thin shock layer behind the bow shock in zone one where the highest temperatures are found and a nonequilibrium model is needed. Strong chemical dissociation reactions of carbon dioxide are found in this area, see figure 18. The mass fractions of atomic oxygen increase rapidly in this area, slowly followed by molecular oxygen which is more present in areas with lower temperatures. The temperatures and chemical relaxations in the jet zone four are dominated by the series of expansion and compression waves, while the relaxation process in zone five is influenced by reflected pressure waves which propagate through the flow field, compare for instance the vibrational temperature in figure 18 with the pressure waves in figure 16 at $t = 3.472 \times 10^{-6}$ s.

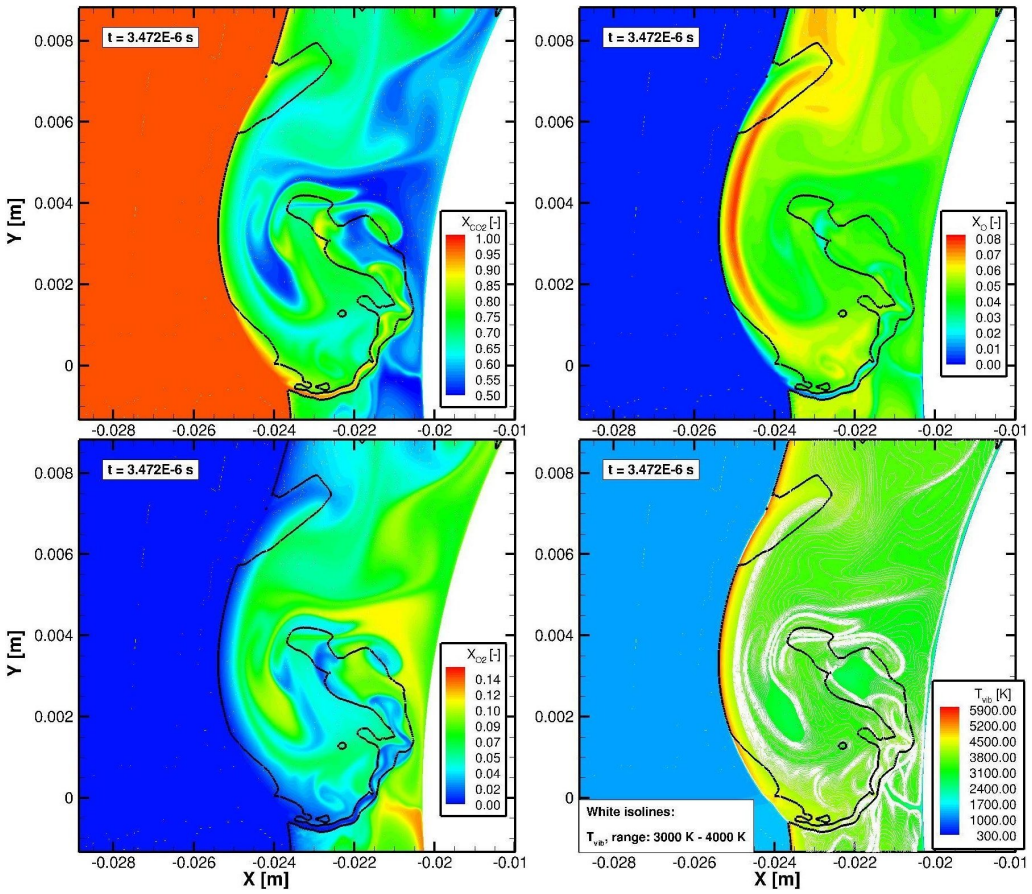

FIGURE 18. Contour plot of mass fractions and vibrational temperature. Jet structure indicated by sonic lines (black).

5.1.3. *Unsteady mechanism*

Yamamoto et al. indicated the unsteadiness of the Edney type VII shock-shock interaction in their publication. This finding can be confirmed for the present configuration, see figure 15. Within the time span of $5 \times 10^{-6}\,s$ captured in the simulation, the supersonic jet expands into the flow field bending around the upper vortex. Only a single large vortex is present in zone seven, which propagates upwards in the flow field. The large vortex in zone six remains almost fixed in a single location, while the medium sized vortices to the upper left and upper right vary significantly in their strength and in their location. In addition, small vortices are formed and shed in the vicinity of the jet contraction zones, see for instance the solution at $t = 0.969 \times 10^{-6}\,s$ in figure 15. The continuous presence of two larger vortices substantiates the strong vorticity of the Edney type VII interaction and is a unique and distinctive feature.

Similar to the test configuration with nitrogen flow, pressure waves originating from the compression and expansion waves in the jet zone four are propagating through the entire flow field. However, unlike in the nitrogen flow configuration where the jet gets close to the wall surface, the pressure waves in the current configuration mostly propagate downstream, see $t = 0.969 \times 10^{-6}\,s$ in figure 16. The pressure waves are reflected at the

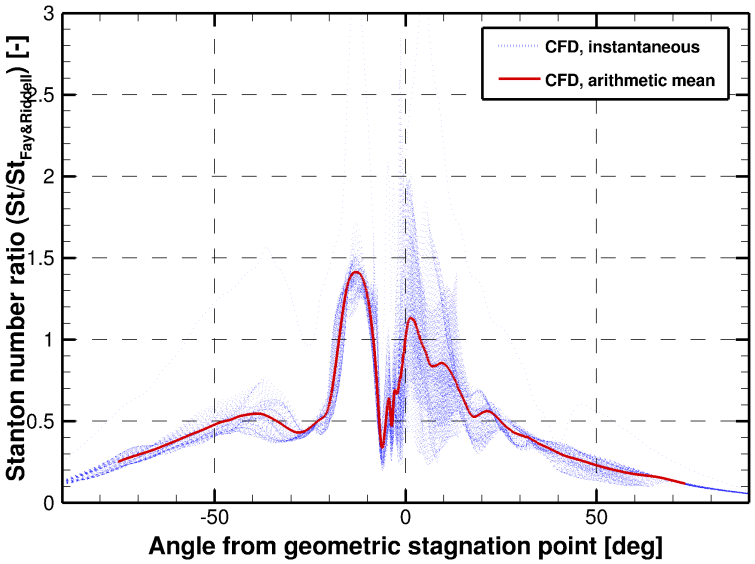

FIGURE 19. Stanton number distribution at the wall for one full cycle of the unsteady mechanism. Output written approximately every 3×10^{-8} s.

wall and propagating upstream, until they hit again the supersonic jet and interact with the downward traveling pressure waves, see for instance $t = 3.472 \times 10^{-6}$ s.

5.2. *Wall Quantities*

The heat flux rates are much lower compared to the nitrogen flow configuration as the jet does not get close to the cylinder surface, let alone, impinge on the wall. The highest Stanton number ratio is found at the beginning of the simulation cycle though the differences are small during the entire simulation, compare figure 19 which indicates that there is a strong clustering of the instantaneous Stanton number ratios around the arithmetic mean.

6. Conclusion

We investigated an Edney type IV shock-shock interaction in its original configuration in nitrogen flow and in a modified version leading to an Edney type VII interaction utilizing a gas model of the Martian atmosphere.

The unsteady mechanism is discussed in detail for the Edney type IV shock-shock interaction. The highly-resolved simulation allows to study the structure and the unsteadiness of the vortices and pressure waves in the entire flow field. A detailed analysis of the jet structure allows to subdivide the jet into six zones and to classify six unsteady mechanisms. The simulation of the flow field and wall quantities at the same time facilitates the description of the influence of the jet unsteady mechanism on the wall heat flux rates. Grid sensitivities are addressed by a multiresolution analysis of the jet un-

steady mechanisms and their interdependency on the grid resolution. A potential pitfall of quasi-steady-state simulation results is identified.

The simulation are repeated utilizing a gas model of the Martian atmosphere. A slightly higher location of the impinging shock wave is selected. The simulations reveal that the Edney type VII interaction, as defined by Yamamoto *et al.* (1999), is an important and pronounced shock-shock interaction for the applied configuration of the Martian atmosphere. The highly-resolved simulation allows to capture the vortex structure and the propagation of pressure wave patterns for this type of shock-shock interaction. The applied multiscale-based grid adaptation concept is beneficial for this configuration, as the unsteady jet structure extends far into the inner flow field and no a-priori knowledge of the flow field is available. The high resolution of the flow field allows to resolve the formation and shedding of small vortices side-by-side with more dominant larger vortex structures. The flow field is subdivided into different zones and the thermochemical relaxation process is analyzed and compared to the nitrogen flow field of the previous configuration. The gained insight into this less known configuration is a helpful basis on which further experimental and theoretical analyses can build.

REFERENCES

Anderson, J.D. 1989 *Hypersonic and High Temperature Gas Dynamics*. New York: McGraw-Hill.

Bird, R. B., Stewart, W. E. & Lightfoot, E. N. 2007 *Transport Phenomena*. John Wiley & Sons, Inc.

Bramkamp, F., Lamby, P. & Müller, S. 2004 An adaptive multiscale finite volume solver for unsteady and steady flow computations. *Journal of Computational Physics* **197**, 460–490.

Capitelli, M., Colonna, G., Giordano, D., Marraffa, L., Casavola, A., Minelli, P.D., Pagano, D., Pietanza, L. & Taccogna, F. 2005*a* High-temperature thermodynamic properties of Mars-atmosphere components. *Journal of Spacecraft and Rockets* **42**, 980–989.

Capitelli, M., Colonna, G., Giordano, D., Marraffa, L., Casavola, A., Minelli, P.D., Pagano, D., Pietanza, L. & Taccogna, F. 2005*b* Tables of internal partition functions and thermodynamic properties of high-temperature Mars-atmosphere species from 50 K to 50000 K. *ESA STR-246* .

Edney, B. 1968 *Anomalous Heat Transfer and Pressure Distributions on Blunt Bodies at Hypersonic Speed in the Presence of Impinging Shocks*. The Aeronautical Research Institute of Sweden: FFA Report 115.

Fay, J.A. & Riddell, F.R. 1958 Theory of stagnation point heat transfer in dissociated air. *Journal of the Aeronautical Sciences* **25** (2), 73–85.

Furumoto, G.H., Zhong, X. & Skiba, J.C. 1996 Unsteady shock-wave reflection and interaction in viscous flow with thermal and chemical nonequilibrium. *34th AIAA Aerospace Sciences Meeeting and Exhibit, AIAA 96-0107* .

Gaitonde, D. 1993 Calculations on unsteady type IV interaction at Mach 8. *Wright Laboratory, WL-TR-93-3002* .

Grasso, F., Purpura, C., Chanetz, B. & Delery, J. 2003 Type III and type IV shock/shock interferences: theoretical and experimental aspects. *Aerospace Science and Technology* **7**, 93–106.

Lamby, P. 2007 *Parametric Multi-Block Grid Generation and Application to Adaptive Flow Simulations*. RWTH Aachen University: PhD Thesis.

Lind, C.A. & Lewis, M.J. 1995 Unsteady characteristics of a hypersonic type IV shock interaction. *Journal of Aircraft* **32** (6), 1286–1293.

Lind, C.A. & Lewis, M.J. 1996 Computational analysis of the unsteady type IV shock interaction of blunt body flows. *Journal of Propulsion and Power* **12** (1), 127–133.

Millikan, R.C. & White, D.R. 1963 Systematics of vibrational relaxation. *General Electric Research Laboratory* .

Müller, S. 2003 *Adaptive Multiscale Schemes for Conservation Laws*, *Lecture Notes on Computational Science and Engineering*, vol. 27. Berlin: Springer.

Olejniczak, J., Wright, M.J. & Candler, G.V. 1997 Numerical study of inviscid shock interactions on double-wedge geometries. *Journal of Fluid Mechanics* **352**, 1–25.

Park, C. 1985 On the convergence of computation of chemically reacting flows. *AIAA paper 085-0247* .

Park, C., Howe, J.T. & Jaffe, R.L. 1994 Review of chemical-kinetic problems of future NASA missions, II: Mars entries. *Journal of Thermophysics and Heat Transfer* **8** (1), 9–23.

Sanderson, S.R. 1995 *Shock Wave Interaction in Hypervelocity Flow*. GALCIT, California Institute of Technology: PhD Thesis.

Sanderson, S.R., Hornung, H.G. & Sturtevant, B. 2004 The influence of non-equilibrium dissociation on the flow produced by shock-impingement on a blunt body. *Journal of Fluid Mechanics* **516**, 1–37.

Stull, D.R. & Prophet, H. 2011 *JANAF thermochemical tables [electronic source]*. National Institute of Standards and Technology.

Windisch, C. 2014 *Efficient Simulation of Thermochemical Nonequilibrium Flows using Highly-Resolved H-Adapted Grids*. RWTH Aachen University: PhD Thesis (submitted).

Windisch, C., Reinartz, B. & Müller, S. 2012 H-adaptive simulation of hypersonic flows in thermochemical nonequilibrium. *18th AIAA/3AF International Space Planes and Hypersonic Systems and Technologies Conference, AIAA 2012-5918* .

Wright, M.J., Tang, C.Y., Edquist, K.T., Hollis, B.R., Krasa, P. & Campbell, C.A. 2010 A review of aerothermal modeling for Mars entry missions. *48th AIAA Aerospace Sciences Meeting, AIAA 2010-0443* .

Yamamoto, S., Takasu, N. & Nagatomo, H. 1999 Numerical investigation of shock/vortex interaction in hypersonic thermochemical nonequilibrium flow. *Journal of Spacecraft and Rockets* **36**, 240–246.